



Modeling the longitudinal variation in the post-sunset far-ultraviolet OI airglow using the SAMI2 model

S. L. England,¹ T. J. Immel,¹ and J. D. Huba²

Received 11 May 2007; revised 11 October 2007; accepted 26 October 2007; published 23 January 2008.

[1] Recent global-scale observations of the low-latitude airglow bands associated with the equatorial ionospheric anomaly (EIA) have revealed a longitudinal variation in the brightness and latitude of the peak airglow emission. For vernal equinox conditions, both of these display a wave number-four pattern when plotted in a constant-local-time frame. It has been proposed that variations in the neutral-wind driven dynamo electric fields from the E-region are responsible for this pattern. Additionally, measurements of the electric fields in the E-region have shown a wave number-four pattern similar to that of the EIA. Here we use the SAMI2 model, that includes a detailed description of ion photochemistry and transport, to demonstrate that the recently observed zonal variations in the E-region dynamo electric fields are sufficient to explain the observed variation in brightness and latitude of the airglow bands for these conditions. The vertical drifts associated with E-region dynamo fields in the SAMI2 model are modified to produce simulations that represent the locations of a maximum and minimum in the wave number-four pattern. The simulated airglow changes such that the brightness of the maximum case is $\sim 40\%$ higher than the peak in the minimum case and the latitude of the peak brightness in the maximum case is located 3° poleward of the peak in the minimum case. Both of these results compare favorably with, and even exceed, the observed variations. This result adds quantitative support to the above stated mechanism. The effect of changes in the drifts at different local time periods on the nighttime airglow is also assessed. It is seen that changes at all local time periods make a significant contribution to the total change in the airglow, with the most significant being close to local noon and during the late afternoon.

Citation: England, S. L., T. J. Immel, and J. D. Huba (2008), Modeling the longitudinal variation in the post-sunset far-ultraviolet OI airglow using the SAMI2 model, *J. Geophys. Res.*, 113, A01309, doi:10.1029/2007JA012536.

1. Introduction

[2] While the peak in ionization rates in the equatorial ionosphere occur at the sub-solar point, the highest plasma densities in the terrestrial system are found in two bands in the *F* region ionosphere, one located either side of the magnetic equator [*Namba and Maeda*, 1939; *Appleton*, 1946]. This feature, known as the equatorial ionospheric anomaly (EIA), is created by an uplift of plasma close to the magnetic equator and the subsequent redistribution of that plasma along magnetic field lines. The electric fields that drive this uplift are generated by dynamo action of winds in the thermosphere at E- and *F* region altitudes (see *Heelis* [2004] for a recent summary).

[3] Airglow emissions associated with the EIA have long been used to study the post-sunset plasma distributions in this region. Global-scale observations of the nighttime far-ultraviolet emissions at 135.6 nm, associated with O^+ recombination, have been made by the IMAGE far-ultraviolet imager (FUV) and the TIMED Global Ultraviolet Imager (GUVI). These emissions come from a range of altitudes, with the brightest from ~ 300 – 450 km [see *Henderson et al.*, 2005b, Figure 2], which corresponds to the *F* region peak.

[4] The large-scale structure of the equatorial airglow arcs have been characterized using these nighttime FUV and GUVI observations [*Sagawa et al.*, 2003, 2005; *Henderson et al.*, 2005a; *Immel et al.*, 2006; *England et al.*, 2006a, 2006b]. These studies have demonstrated that the brightness and magnetic latitude of the airglow peaks in a fixed local-time frame vary with longitude in a wave-like pattern with a zonal wave number of four. *Immel et al.* [2006] showed that these variations correlate well with variations in the E-region winds associated with the non-migrating eastward wave number-3 diurnal tide (DE3). *England et al.* [2006b] went on to show that the noontime equatorial electrojet (EEJ) in the E-region ionosphere also exhibits the same

¹Space Sciences Laboratory, University of California Berkeley, Berkeley, California, USA.

²Plasma Physics Division, Naval Research Laboratory, Washington, District of Columbia, USA.

Table 1. Numerical Values and Definitions of the Coefficients Used in Equation (1)

α_{1356}	Radiative recombination rate @ 1160 K	7.3×10^{-13}
β_{1356}	Ion-ion neutralization yield	0.54
k_1	Radiative attachment	1.3×10^{-15}
k_2	Ion-ion neutralization rate	10^{-7}
k_3	Ion-atom neutralization rate	1.4×10^{-10}

longitudinal modulation, lending support to the theory that the E-region dynamo winds are responsible for creating the observed variation in the post-sunset airglow emissions. However, while the both *Immel et al.* [2006] and *England et al.* [2006b] detailed a plausible mechanism to explain the airglow observations, neither work attempted to demonstrate that the tidal amplitudes were sufficient to explain the observed changes in the airglow brightness and location.

[5] Recently, *Hagan et al.* [2007] have simulated this mechanism in a general circulation model, inputting the DE3 close to its source in the lower atmosphere and calculating the effect on the post-sunset [e^-] in the model. The authors successfully demonstrated that the DE3 is capable of producing a longitudinal variation in the [e^-] that is similar to that inferred from the 135.6 nm airglow observations, although some differences were noted.

[6] There is still a need to demonstrate that the changes in the E-region dynamo fields are sufficient to produce the observed changes in the 135.6 nm airglow, taking into account ion production, transport, non-radiative loss mechanisms and radiative recombination. Here this issue is addressed using the NRL ionosphere model SAMI2 (Sami2 is Another Model of the Ionosphere, [*Huba et al.*, 2000]), that simulates the above effects. In an alternative approach to the fully self-consistent model of *Hagan et al.* [2007], we shall introduce a perturbation to the inputs to the SAMI2 model that is based solely on the observations of the varying E-region currents reported by *England et al.* [2006b]. This has the advantage over the approach by *Hagan et al.* [2007] in that the amplitude of the perturbation we introduce to the model is well constrained by observations. In order to quantitatively compare the SAMI2 output with the observations of TIMED GUVI, we shall also describe an addition to this model that allows us to simulate the 135.6 nm airglow brightness that would be observed for the simulated ionosphere-thermosphere system. Using the SAMI2 model also allows us to calculate the contribution made to the overall change in the simulated 135.6 nm airglow brightness by changes in the E-region fields during different periods of the day. This will allow us to determine which local time periods are most significant in producing the simulated changes in the post-sunset airglow.

2. SAMI2 Simulations and Results

[7] SAMI2 is a two-dimensional, first principles model of the low- and midlatitude ionosphere. A full description and complete source code for model is freely available at <http://wwwppd.nrl.navy.mil/sami2-OSP/index.html>. The important aspects of this model for the present study are the following: (1) SAMI2 includes a detailed description of O^+ photochemistry and transport, and (2) the $E \times B$ vertical drifts in the F region are not calculated self-consistently from the E- and F region neutral winds and ion densities,

but are specified using the *Scherliess and Fejer* [1999] empirical model. This allows a change in the $E \times B$ drifts to be externally imposed, that is essential for the present study.

[8] In order to calculate the airglow brightness which correspond to the simulated ionosphere-thermosphere system in SAMI2, it is necessary to introduce a calculation of the line-of-sight-integrated airglow brightness. For the 135.6 nm emission from OI, the total brightness (in Rayleighs) is given by

$$I_{RR} = \frac{1}{10^6} \int \alpha_{1356}(T_e) N_e [O^+] ds + \frac{\beta_{1356} k_1 k_2}{10^6} \int \frac{N_e [O] [O^+]}{k_2 [O^+] + k_3 [O]} ds. \quad (1)$$

[9] The above equation describes the emission created by both radiative recombination of O^+ (first term) and the minor contribution due to mutual neutralization of O^+ and O^- (second term). The coefficients in the above equation are defined and their numerical values given in Table 1. All values are based on the work of *Meléndez-Alvira et al.* [1999] and references therein. A simple examination of this equation shows that the brightness of the 135.6 nm airglow is not only a function of the total column amount of O^+ , but also its spatial distribution, the electron temperature (through α_{1356}), and to a lesser degree [O]. This means that is not easy to quantitatively transform the observed 135.6 nm brightness into a measure of the ionospheric density without additional supporting information that are often not simultaneously measured. Conversely, each of these parameters are either calculated by, or in the case of [O], explicitly specified in SAMI2, making the reverse calculation straightforward.

[10] The observations of the noontime EEJ around equinox reported by *England et al.* [2006b] show that the peak sheet current density (which is a good measure of the E-region equatorial eastward electric field) varies as a function of longitude, with four peaks at $\sim 90^\circ$ spacing. From the observations of the CHAMP satellite, it can be seen that the maxima in the current densities are on average 63% higher than the minima (similar variations were also reported for SAC-C and Ørsted observations in the same work). Here we shall assume that this corresponds to a $\sim 60\%$ increase in the strength of the eastward electric field and drifts associated with the equatorial E-region at these locations. Recently *Hartman and Heelis* [2007] have measured the longitudinal variation in the vertical drifts at 09:30 LT and ~ 830 km altitude using the ion drift meter onboard Defense Meteorological Satellite Program (DMSP) F15 during 2001 and 2002. It is worth noting here that while a wave number-four pattern is not always clear in these observations, the increase in the drift speed often exceeds 60% when the pattern is observed.

[11] We present results from two simulations using SAMI2. The first, which we shall refer to as the Max case, is a standard SAMI2 simulation for day 90 of 2002, which corresponds to the same time frame as the airglow observations presented in *England et al.* [2006b]. This simulation is for moderate-to-high solar activity ($F10.7 = 181 \times 10^{-22} \text{ Js}^{-1} \text{ m}^{-2} \text{ Hz}^{-1}$) and low-to-moderate geomagnetic activity ($A_p = 21$), that corresponds to the conditions present during the GUVI observations. This simulation is intended to represent the conditions at one of the peaks in the wave number-four pattern described

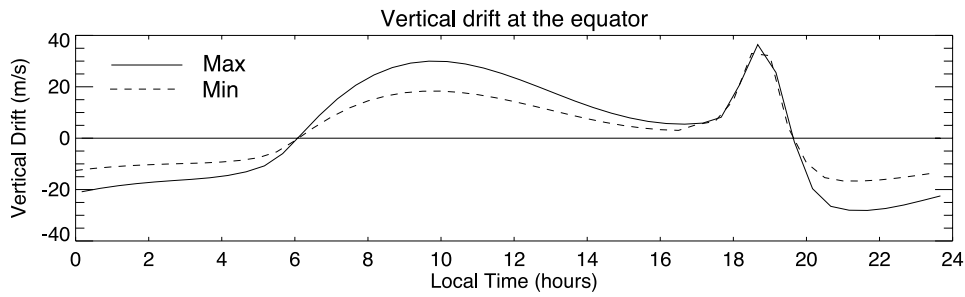


Figure 1. Equatorial vertical drifts used in the SAMI2 model simulations as a function of local time at 190° longitude.

earlier and therefore we perform our simulation at 190° geographic longitude. This corresponds to the location of the observed peak where the geographic latitude and declination of the magnetic equator is smallest. Choosing this longitude section therefore also has the advantage that any effects relating to these geometric parameters are minimized, thus reducing the number of effects that must be considered in the interpretation of our results.

[12] Our second simulation (referred to as the Min case) uses the same input conditions as the Max case, except that we introduce a perturbation to the $E \times B$ drift prescribed in the model. This is shown in Figure 1. In order to modify the $E \times B$ drifts in the *Scherliess and Fejer* [1999] model to represent the drift at one of the minima in the wave number-four pattern, we decrease the strength of the $E \times B$ drift by 40% during all local time periods when the drift is dominated by the E-region fields. Around the time of the post-sunset rise (here 17:00–19:30 LT) the *F* region dynamo fields dominate. As the *F* region dynamo fields are not expected to be modulated by the DE3 tide, these $E \times B$ drifts are left unchanged.

[13] Figure 2 shows the vertical total electron content (TEC) and nadir 135.6 nm airglow at 21:00 LT simulated by SAMI2. Comparing the Max and Min cases, it can be seen that both the simulated TEC and airglow brightness are greater for the Max case than the Min. For the simulated

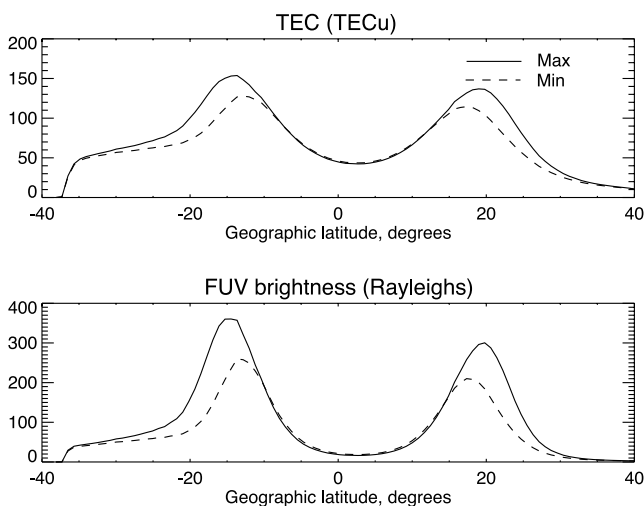


Figure 2. Vertical TEC and nadir 135.6 nm airglow brightness as a function of latitude from the SAMI2 model simulations at 190° longitude and 21:00 LT.

airglow emissions, the peak brightness in the Max case is 39% and 43% higher than in the Min case for the northern and southern airglow bands respectively. The peak airglow emission and peak TEC are also located at higher latitudes for the Max case than the Min. For the case of the simulated airglow emissions, the peak in the Max case is located 3° poleward of the peak in the Min case in both hemispheres.

[14] While it is not strictly consistent with the experiment described above, it is instructive to also calculate the contribution from different local time sectors to the total enhancement in the *F* region shown in Figure 2. To do this we perform an additional test, in which we switch between the Max and Min $E \times B$ drifts at different local times throughout the day. For these simulations, the Min drifts are used as the control. The Max drifts are used from sunrise until the desired local time, following which the Min drifts are used. Figure 3 shows the simulated peak 135.6 nm airglow brightness at 21:00 LT in the northern airglow band as a function of the local time until which the Max drifts are used. As the Max drifts are applied for progressively longer periods throughout the day an increase in the simulated nighttime airglow brightness is seen. The largest increase is for local times around noon and in the late afternoon and the smallest is for the early morning.

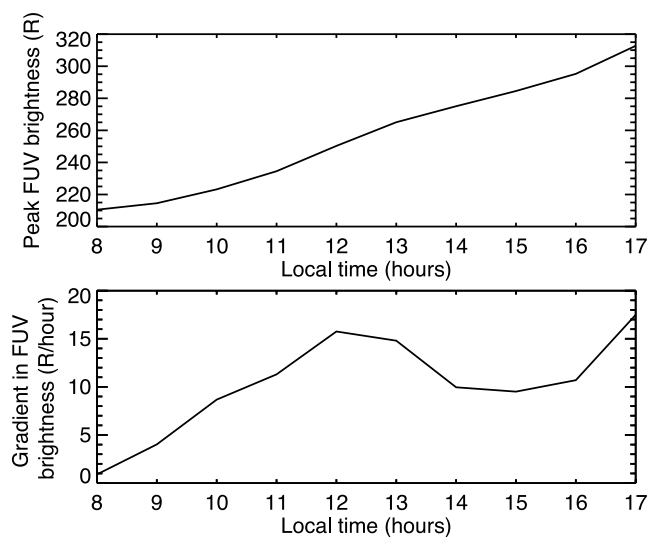


Figure 3. (top) Peak simulated FUV brightness in the northern airglow arc at 21:00 LT as a function of the local time until which the enhancement in the electric fields is applied. (bottom) Change in the peak simulated FUV brightness with local time. See text for details.

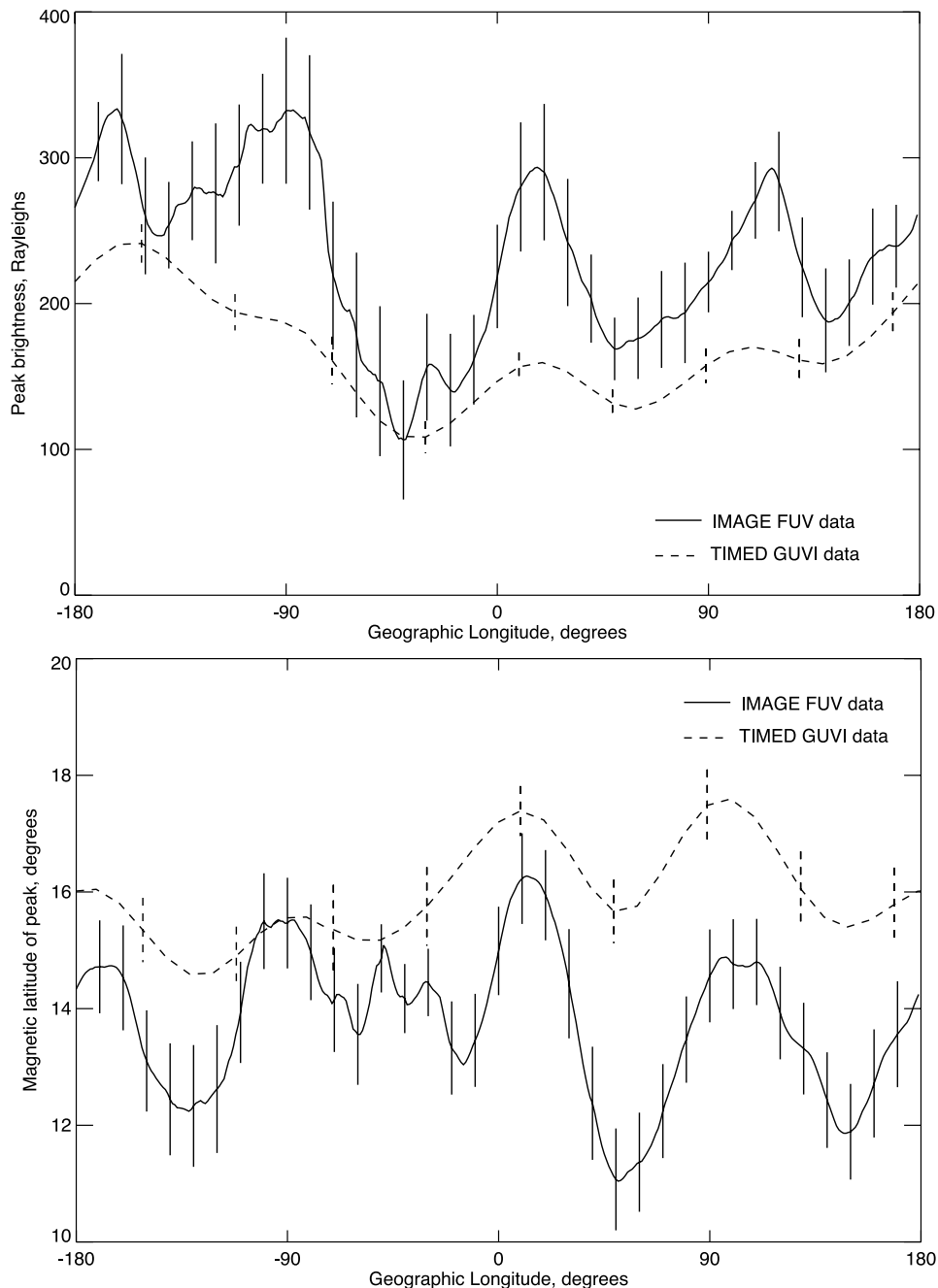


Figure 4. (top) The maximum brightness of the 135.6 nm emission and (bottom) the magnetic latitude of the maximum brightness observed in the northern arc of the EIA by IMAGE FUV (solid) and TIMED GUVI (dashed). Values have been averaged with a 10-degree running mean and assume a mean emission altitude of 350 km. All data come from 20:30 to 21:30 LT, during magnetically quiet periods from March and April 2002. Figure after *England et al.* [2006b].

The variation with local time of the southern airglow band and the TEC variations (not shown) show similar behaviors. Beyond 17:00 LT, the drifts associated with the pre-reversal enhancement begin to dominate the $E \times B$ drift pattern, so variations are not applied after this local time.

3. Discussion

[15] Further consideration of equation (1) highlights that the line-of-sight direction has a great impact on the ob-

served airglow intensity. As discussed in *England et al.* [2006a], the IMAGE FUV observations come from a range of observing angles and while the authors made some attempt to correct for this, the assumptions required for this correction are not ideal. A more reliable measure for a quantitative comparison between the observed and simulated airglow brightness is to compare the simulated values with the nadir-only observations by TIMED GUVI, shown in Figure 4 (after [*England et al.*, 2006b]). In addition to being nadir-only observations, the analysis technique used here

[Henderson *et al.*, 2005a] also explicitly removes the effects of plasma bubbles on the observed airglow brightness.

[16] Figure 4 shows the northern hemisphere airglow band at 21:00 LT observed by TIMED GUVI for the vernal equinox of 2002. At 190° longitude, the observed airglow brightness was 220 R in the northern hemisphere. This is lower than the simulated brightness in our Max case (300 R), which is intended to simulate the conditions present at this longitude and for this time period. This means that the SAMI2 model is simulating a denser *F* region ionosphere than was present during the observational period.

[17] Figure 4 shows a mean observed increase in airglow brightness of 28% at the locations of the maxima compared with the minima. In addition, the mean latitude of the peak airglow emissions at the maxima are 1.5° poleward of those at the minima. These values compare favorably with the changes simulated using SAMI2, although once again the simulated values are larger than those observed. We therefore conclude that when a detailed consideration of ion production, loss and transport is taken into consideration, the changes in the E-region fields reported by England *et al.* [2006b] are more than sufficient to account for the observed variation in the nadir airglow brightness and distribution. This result adds substantial weight to the mechanism proposed by Immel *et al.* [2006], which states that changes in the E-region dynamo associated with changes in the winds driving that dynamo are responsible for the observed longitudinal variation in the low-latitude airglow bands.

[18] Figure 3 shows that changes in the $E \times B$ drifts at all local times throughout the day contribute to the total change simulated in the *F* region. As may be expected, the enhancement in the drifts close to sunrise (before 10:00 LT), when the total $E \times B$ drift is small, create little change in the airglow brightness simulated at 21:00 LT. The $E \times B$ drifts in the late afternoon are also small, but as these occur closer to 21:00 LT, loss mechanisms have less of an effect and so these drifts at this time are seen to be more important than those before 10:00 LT. Additionally, the enhancement in the drifts around noon, when both the $E \times B$ drifts and photo-ionization rates maximize, are seen to produce a large variation in the airglow brightness at 21:00 LT. Thus the change in the $E \times B$ drifts at no single local time period are seen to dominate the change in the airglow brightness simulated at 21:00 LT.

[19] Future studies using the SAMI3 model may be able to address the details of the three-dimensional, time-varying perturbation to the E-region fields created by DE3, the possible impact of coupling between the E- and *F* region dynamos via modulation of the *F* region Pedersen conductivities, the seasonal and longitudinal effects on E-region dynamo-*F* region airglow coupling, the explanation of the large day-to-day variations observed in the longitudinal structure of the airglow, the effects of variations in the dynamo fields across the E-region and also to compare the

changes in the daytime ionosphere and the daytime vertical TEC measurements made by GPS occultation.

[20] **Acknowledgments.** This work was supported by the NASA Living With a Star program through the grant NNX07AT80G. JDH was supported by ONR.

[21] Amitava Bhattacharjee thanks Mangalathayil Ali Abdu and John Meriwether for their assistance in evaluating this paper.

References

- Appleton, E. (1946), Two anomalies in the ionosphere, *Nature*, *157*, 691.
- England, S. L., T. J. Immel, E. Sagawa, S. B. Henderson, M. E. Hagan, S. B. Mende, H. U. Frey, C. M. Swenson, and L. J. Paxton (2006a), The effects of atmospheric tides on the morphology of the quiet-time, post-sunset equatorial ionospheric anomaly, *J. Geophys. Res.*, *111*, A10S19, doi:10.1029/2006JA011795.
- England, S. L., S. Maus, T. J. Immel, and S. B. Mende (2006b), Longitudinal variation of the E-region electric fields caused by atmospheric tides, *Geophys. Res. Lett.*, *33*, L21105, doi:10.1029/2006GL027465.
- Hagan, M., A. Maute, R. G. Roble, A. D. Richmond, T. Immel, and S. England (2007), Connections between deep tropical clouds and the Earth's ionosphere, *Geophys. Res. Lett.*, *34*, L20109, doi:10.1029/2007GL030142.
- Hartman, W. A., and R. A. Heelis (2007), Longitudinal variations in the equatorial vertical drift in the topside ionosphere, *J. Geophys. Res.*, *112*, A03305, doi:10.1029/2006JA011773.
- Heelis, R. A. (2004), Electrodynamics in the low and middle latitude ionosphere: A tutorial, *J. Atmos. Terr. Phys.*, *66*, 825–838.
- Henderson, S. B., C. M. Swenson, A. B. Christensen, and L. J. Paxton (2005a), Morphology of the equatorial anomaly and equatorial plasma bubbles using image subspace analysis of Global Ultraviolet Imager data, *J. Geophys. Res.*, *110*, A11306, doi:10.1029/2005JA011080.
- Henderson, S. B., C. M. Swenson, J. H. Gunther, A. B. Christensen, and L. J. Paxton (2005b), Method for characterization of the equatorial anomaly using image subspace analysis of Global Ultraviolet Imager data, *J. Geophys. Res.*, *110*, A08308, doi:10.1029/2004JA010830.
- Huba, J. D., G. Joyce, and J. A. Fedder (2000), Sami2 is Another Model of the Ionosphere (SAMI2): A new low-latitude ionosphere model, *J. Geophys. Res.*, *105*, 23,035–23,054.
- Immel, T. J., E. Sagawa, S. L. England, S. B. Henderson, M. E. Hagan, S. B. Mende, H. U. Frey, C. M. Swenson, and L. J. Paxton (2006), Control of equatorial ionospheric morphology by atmospheric tides, *Geophys. Res. Lett.*, *33*, L15108, doi:10.1029/2006GL026161.
- Meléndez-Alvira, D. J., R. R. Meier, J. M. Picone, P. D. Feldman, and B. M. McLaughlin (1999), Analysis of the oxygen nightglow measured by the Hopkins Ultraviolet Telescope: Implications for ionospheric partial radiative recombination rate coefficients, *J. Geophys. Res.*, *104*, 14,901–14,914.
- Namba, S., and K.-I. Maeda (1939), *Radio Wave Propagation*, p. 86, Corona Publishing, Tokyo.
- Sagawa, E., T. Maruyama, T. J. Immel, H. U. Frey, and S. B. Mende (2003), Global view of the nighttime low-latitude ionosphere by the IMAGE/FUV 135.6 nm observations, *Geophys. Res. Lett.*, *30*(10), 1534, doi:10.1029/2003GL017140.
- Sagawa, E., T. J. Immel, H. U. Frey, and S. B. Mende (2005), Longitudinal structure of the equatorial anomaly in the nighttime ionosphere observed by IMAGE/FUV, *J. Geophys. Res.*, *110*, A11302, doi:10.1029/2004JA010848.
- Scherliess, L., and B. G. Fejer (1999), Radar and satellite global equatorial *F* region vertical drift model, *J. Geophys. Res.*, *104*, 6829–6842.
- S. L. England and T. J. Immel, Space Sciences Laboratory, University of California Berkeley, Berkeley, CA 94720, USA. (england@ssl.berkeley.edu)
- J. D. Huba, Plasma Physics Division, Naval Research Laboratory, Washington, D.C. 20375, USA.